

An Approach for the Reduction of Boundary Effects in Time-Frequency Representations

Adrien Meynard, Hau-Tieng Wu

Abstract—Time-frequency representations are intrinsically subject to the boundary effects. As a consequence, the structures of signals that are highlighted by the representations are garbled when approaching the boundaries of the time-frequency domain. In this paper, we propose an approach for the reduction of such boundary effects, whose objective is to be able to be used in real time. That one relies on an extension of the analyzed signal obtained by a forecasting technique. In the case of the study of a class of locally oscillating signals, we provide a theoretical study of the performance of our approach. Following a numerical verification of the performance of the algorithm, we implement it on real-life biomedical signals.

Index Terms—Boundary effects, time-frequency, forecasting

I. INTRODUCTION

IN any digital acquisition system, the study and the interpretation of the measured signals generally require the use of an analysis tool, which enable to point out the useful characteristics of the signal. This problem arises for the analysis of signals as varied as audio [1], [2], mechanical [3] or biomedical signals [4]. For instance, any measured biomedical signal, such as photoplethysmogram (PPG), may not be interpreted as it is, from its run chart. An analysis tool would make possible the extraction of some useful characteristics such as heart rate or blood pressure.

In general, the observed quantities are produced by transient phenomena, that can vary rapidly and irregularly. As a consequence, the measured signals exhibit nonstationary behavior. In order to adapt the analysis to nonstationarities, local spectral analysis is generally performed [5], [6]. The short time Fourier transform [7] (STFT) is a typical tool which is build that way, and enables the determination of the local frequency content of a nonstationary signal.

Windowing is a common method for performing local analysis. Among others, STFT, wavelet transform [8], synchrosqueezing transform (SST), and reassignment [9] (RS) are representations that fall back on the use of an analysis window. Let $x : I \rightarrow \mathbb{R}$ denote the observed signal, where I denotes the finite interval where the signal is measured. Let $g_s : \mathbb{R} \rightarrow \mathbb{R}$ denote the analysis window, where s is a shape parameter. The support of

g_s is localized around the origin, and is small with respect to $|I|$. The translation operator is T_τ defined as:

$$T_\tau f = f(t - \tau), \quad \forall f : \mathbb{R} \rightarrow \mathbb{R}.$$

Then, the local analysis of x around the instant $\tau \in I$ rely on the evaluation of the following dot product:

$$V_x(s, \tau) = \langle x, T_\tau g_s \rangle_I. \quad (1)$$

A major shortcoming of this technique occurs when analyzing the signal x near the boundaries of the interval I . Indeed, at these points, half of the information is missing. Consequently the results of the dot product 1 is disturbed by this lack of information. This phenomenon is the so-called *boundary effect*. We display, on the left of Fig. 1 the result of the SST of a PPG (see section IV-B3 for a comprehensive description). The distortion resulting from boundary effects is clearly visible on both sides of this representation. Indeed, while in the major central part of the image, clear lines stand out, they become blurred as they approach the left and right boundaries of the image. A zoom on the right boundary of this SST, displayed on the right of Fig. 1, emphasizes the result of boundary effects. More generally, estimations of signal characteristics, like instantaneous frequencies [10] or amplitudes, from its time-frequency representation appear to be imprecisely determinable (or even likely to fail) in the vicinity of the boundaries.

The purpose of this paper is to provide a fast algorithm allowing to tackle boundary effects and limit the disruptions it may cause on the signals representations based on windowing. Attempts to minimize the boundary effects generally consists in softening the discontinuity on signals edges. For instance, judicious choices of analysis windows whose support does not interfere with the boundary points can minimize the occurrence of aberrant patterns near the boundaries of the time-frequency plane [11], [12]. These techniques therefore do not make it possible to reduce the boundary effects of any time-frequency representations, and for any analysis window. For this purpose, a natural idea consists in carrying out a preliminary step to the analysis allowing to extend the signal beyond its boundaries. Hence, to implement our boundary effects reduction procedure, we proceed in two steps.

- 1) *Extend the signal by forecasting it.* The aim is to use a dynamic model to predict the values taken by the measured signal outside the measurement interval.

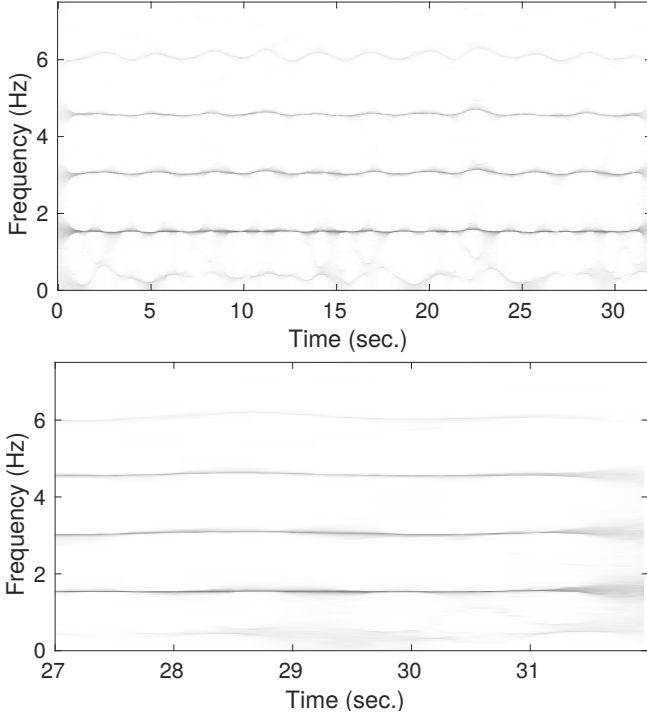


Figure 1. Synchrosqueezing transform of a PPG (top) with a zoom on its right boundary (bottom).

Then, once this operation is done, we have access to an extended signal defined on a larger interval I_Δ , where Δ denotes the size of the extension on both boundaries of I .

- 2) *Run the local analysis tool on the extended signal.* Assuming that the support of the analysis window is smaller than 2Δ , the local analysis near the boundary of I is now possible without lack of information thanks to knowledge brought by the extension on both sides.

Thus, assuming that the quality of the extension step is sufficient, the representation obtained that way will be less sensitive to the boundary effects than the result of the analysis tool applied directly to the non-extended signal.

Various extension schemes have been proposed. On one hand, there exists simple extension schemes that do not take into account the dynamical behavior of the signal, such as zero-padding, periodic extension, symmetric extension [13], [14], or polynomial extrapolation [15]. On the other hand, there exists extension schemes based on physically relevant dynamical models, such as the Extended Dynamic Mode Decomposition [16] (EDMD), the Gaussian process regression [17], [18] (GPR), the TBATS algorithm [19]. While the second class of extension schemes give better extended signals than the first class, they generally have a great computational cost. We propose here a fast extension algorithm based on a simple dynamical model, in order to optimize the trade-off between the extension quality and the computational cost. Furthermore, we prove that the dynamical model

we consider is sufficient to forecast locally oscillating signals.

Therefore, in section II, we provide an extension method based on a linear dynamic model. We derive the corresponding algorithm for boundary effects reduction. In section III, we show that, even though we consider a simplistic dynamic model, it is sufficient to extend signals taking the form of sums of sine waves. An evaluation of the theoretical performance of our algorithm on a class of signals, the sums of sine waves, is given in section III. In section IV, we compare our extension method with more sophisticated methods such as EDMD, GPR, or TBATS. We show that our algorithm gives fast results of reasonable quality. Finally, we evaluate the performance of our boundary effects reduction algorithm on biomedical signals such as respiratory signals, and compare it to the theoretical results.

II. ALGORITHM

As explained above, the algorithm for the reduction of boundary effects on time-frequency representations relies on two steps. These ones are detailed in the current section.

A. Forecasting

Let $x : \mathbb{R} \rightarrow \mathbb{R}$ denote a continuous-time signal. In this work, we consider a finite-length discretization of that one. Thus, the sampled signal \mathbf{x} , whose length is denoted by N , is such that

$$\mathbf{x}[n] = x\left(\frac{n}{f_s}\right), \quad \forall n \in \{0, \dots, N-1\},$$

where f_s denotes the sampling frequency.

a) *Notations:* Let M and K be two integers such that $M < N$ and $K + M < N$. Then, for all $k \in \{0, \dots, K-1\}$, we extract from $\mathbf{x} \in \mathbb{R}^N$ the sub-signal $\mathbf{x}_k \in \mathbb{R}^M$ given by:

$$\mathbf{x}_k = \begin{pmatrix} \mathbf{x}[N - K + (k - 1) - (M - 1)] \\ \vdots \\ \mathbf{x}[N - K + (k - 1)] \end{pmatrix}. \quad (2)$$

These sub-signals are gathered into the matrix $\mathbf{X} \in \mathbb{R}^{M \times K}$ such that:

$$\mathbf{X} = (\mathbf{x}_0 \quad \dots \quad \mathbf{x}_{K-1}).$$

Notice that these sub-signals are overlapping each other. Indeed, \mathbf{x}_{k+1} is a shifting of \mathbf{x}_k from one sample. We also consider the matrix $\mathbf{Y} \in \mathbb{R}^{M \times K}$ given by:

$$\mathbf{Y} = (\mathbf{x}_1 \quad \dots \quad \mathbf{x}_K).$$

b) *Dynamical model and forecasting*: Establishing a dynamical model consists in determining the relation linking \mathbf{Y} to \mathbf{X} , that is finding a function f so that

$$\mathbf{Y} = f(\mathbf{X}) .$$

In a general framework, forecasting means estimating the function f from the observed values taken by the signal, in order to predict its future values. For instance, the dynamic mode decomposition [20], [16] allows this by setting very few additional constraints on the regularity of f . We will see later, in section III, that it is not necessary to consider such a complex dynamic model for the study of the signals of interest to us. That is why we consider here a naive dynamical model, assuming that we have the following relation:

$$\mathbf{Y} = \mathbf{A}\mathbf{X} , \quad (3)$$

where $\mathbf{A} \in \mathbb{R}^{M \times M}$. We adopt a classical strategy in the study of dynamical systems, that is the linearization of a nonlinear phenomenon. Notice that this linear dynamical model can be written equivalently in function of the sub-signals \mathbf{x}_k , as:

$$\mathbf{x}_{k+1} = \mathbf{A}\mathbf{x}_k , \forall k \in \{0, \dots, K-1\} . \quad (4)$$

The forecasting method consists in estimating the unknown matrix \mathbf{A} . Indeed, let $\tilde{\mathbf{A}}$ denotes the estimate of \mathbf{A} , we then obtain the forecasting of the signal at time $\frac{N-1+\ell}{f_s}$ by:

$$\tilde{\mathbf{x}}[N-1+\ell] = \boldsymbol{\alpha}^{(\ell)} \mathbf{x}_K , \quad (5)$$

where $\boldsymbol{\alpha}^{(\ell)}$ denotes the last row of $\tilde{\mathbf{A}}^\ell$, that is to say:

$$\boldsymbol{\alpha}^{(\ell)} = \mathbf{e}_M^T \tilde{\mathbf{A}}^\ell , \quad (6)$$

where \mathbf{e}_M is the vector of length M given by $\mathbf{e}_M = (0 \dots 0 \ 1)^T$.

c) *Model estimation*: To estimate the matrix \mathbf{A} , we basically implement the least square estimator. Thus, we solve the following problem:

$$\tilde{\mathbf{A}} = \arg \min_{\mathbf{A}} \mathcal{L}(\mathbf{A}) , \quad (7)$$

where the loss function \mathcal{L} is given by:

$$\mathcal{L}(\mathbf{A}) = \|\mathbf{Y} - \mathbf{A}\mathbf{X}\|^2 = \sum_{k=0}^{K-1} \|\mathbf{x}_{k+1} - \mathbf{A}\mathbf{x}_k\|^2 .$$

Therefore, solving the problem (7), i.e. $\nabla \mathcal{L}(\tilde{\mathbf{A}}) = \mathbf{0}$, gives the following estimate $\tilde{\mathbf{A}}$ of the dynamical model matrix \mathbf{A} :

$$\tilde{\mathbf{A}} = \mathbf{Y}\mathbf{X}^T(\mathbf{X}\mathbf{X}^T)^{-1} . \quad (8)$$

Remark 1. This expression clearly shows that the matrix $\tilde{\mathbf{A}}$ takes the following form:

$$\tilde{\mathbf{A}} = \begin{pmatrix} 0 & 1 & 0 & \dots & 0 \\ \vdots & \ddots & \ddots & \ddots & \vdots \\ \vdots & & \ddots & \ddots & 0 \\ 0 & \dots & \dots & 0 & 1 \\ \alpha_1 & \dots & \dots & \dots & \alpha_M \end{pmatrix} .$$

Then, except the row vector $\boldsymbol{\alpha} = (\alpha_1 \dots \alpha_M)$, the matrix \mathbf{A} is fully determined by the dynamical model.

d) *Signal extension*: In order to reduce the boundary effects on both "sides" of the time-frequency (or time-scale) representation, we finally construct the extended signal $\tilde{\mathbf{x}} \in \mathbb{R}^{N+2L}$ concatenating the backward prediction $\tilde{\mathbf{x}}_{\text{bw}}$, the observed signal \mathbf{x} , and the forward prediction $\tilde{\mathbf{x}}_{\text{fw}}$. We summarize the extension step in Algorithm 1. Notice that we handle the backward estimation using the same strategy than described above, but applying it to the reverse signal $\mathbf{x}^r = (\mathbf{x}[N-1] \dots \mathbf{x}[0])^T$.

Algorithm 1 Signal extension. $\tilde{\mathbf{x}} = \text{SigExt}(\mathbf{x}, M, K, L)$

Inputs: \mathbf{x}, M, K, L

Forward forecasting.

- LS estimation of the forward matrix $\tilde{\mathbf{A}}_{\text{fw}}$ via equation (8).
- Forward forecasting $\tilde{\mathbf{x}}_{\text{bw}}$ obtained applying equation (5) with $\ell \in \{1, \dots, L\}$.

Backward forecasting.

- Reverse signal \mathbf{x} to \mathbf{x}^r .
- LS estimation of the backward matrix $\tilde{\mathbf{A}}_{\text{bw}}$ via equation (8) applied to \mathbf{x}^r .
- Reversed backward forecasting $\tilde{\mathbf{x}}_{\text{bw}}^r$ obtained applying equation (5) to \mathbf{x}^r with $\ell \in \{1, \dots, L\}$.
- Reverse $\tilde{\mathbf{x}}_{\text{bw}}^r$ to obtain the estimate $\tilde{\mathbf{x}}_{\text{bw}}$.

Output: Extended signal $\tilde{\mathbf{x}} = (\tilde{\mathbf{x}}_{\text{bw}} \ \mathbf{x} \ \tilde{\mathbf{x}}_{\text{fw}})^T$.

B. Representation

Let $\mathcal{F}_N : \mathbb{R}^N \rightarrow \mathbb{R}^{F \times N}$ generically denotes the time-frequency or time-scale representation we are interested in. It can be, for instance, such as short-time Fourier transform (STFT), the continuous wavelet transform (CWT), the synchrosqueezing transform (SST), or the reassignment (RS). Here, F typically denotes the size of the representation along the frequency axis. Due to the boundary effects, the representation $\mathcal{F}_N(\mathbf{x})$ shows undesired patterns when approaching its edges. For example, the instantaneous frequencies highlighted by the SST can be blurred near that edges. To limit these phenomena, we apply the representation to the estimated extended signal $\tilde{\mathbf{x}}$. This strategy moves the boundary effects out of the time interval $I = [0, \frac{N-1}{f_s}]$. Finally, the boundary-effects insensitive representation $\mathcal{F}_N^{\text{ext}} : \mathbb{R}^N \rightarrow \mathbb{R}^{F \times N}$ of \mathbf{x} is given for all $v \in \{0, \dots, F-1\}$, $n \in \{0, \dots, N-1\}$ by:

$$\mathcal{F}_N^{\text{ext}}(\mathbf{x})[v, n] = \mathcal{F}_{N+2L}(\tilde{\mathbf{x}})[v, L+n] . \quad (9)$$

This amounts to restricting the representation $\mathcal{F}_{N+2L}(\tilde{\mathbf{x}})$ to the original measurement interval of \mathbf{x} . For the sake of simplicity, we denotes the restriction operator by \mathcal{R} , where $\mathcal{R} : \mathbb{R}^{F \times (N+2L)} \rightarrow \mathbb{R}^{F \times N}$. Consequently, we have:

$$\mathcal{F}_N^{\text{ext}}(\mathbf{x}) = \mathcal{R}(\mathcal{F}_{N+2L}(\tilde{\mathbf{x}})) .$$

C. Global algorithm

Finally, the global procedure we implement to reduce boundary effects on windowing-based representations is summarized by the pseudo-code of Algorithm 2.

Algorithm 2 Tackling boundary effects. $\mathbf{F}_x = \text{BoundEffRed}(\mathbf{x}, M, K, L, \mathcal{F})$

Inputs: $\mathbf{x}, M, K, L, \mathcal{F}$

Forecasting step.

- Signal extension: $\tilde{\mathbf{x}} = \text{SigExt}(\mathbf{x})$.

Representation step.

- Representation evaluation: $\mathcal{F}_{N+2L}(\tilde{\mathbf{x}})$.
- Restriction of $\mathcal{F}_{N+2L}(\tilde{\mathbf{x}})$ to the central time interval (see (9)) to obtain $\mathbf{F}_x = \mathcal{F}_N^{\text{ext}}(\mathbf{x})$.

Output: Signal representation \mathbf{F}_x

III. THEORETICAL PERFORMANCE

A. Signal model

We model the deterministic part of the observed signal as a multicomponent harmonic signal, that is a sum of sine waves. Then:

$$\mathbf{z}[n] = \sum_{j=1}^J \Omega_j \cos\left(2\pi f_j \frac{n}{f_s}\right), \quad (10)$$

where J denotes the number of components, Ω_j the amplitude of the j -th component, and f_j its frequency.

Remark 2. For the sake of simplicity, we make an additional assumption on the frequencies of each component. We assume that for all $j \in \{1, \dots, J\}$:

$$\exists p_j, p'_j \in \mathbb{N}^* : f_j = \frac{p_j}{M} f_s = \frac{p'_j}{K} f_s. \quad (11)$$

In addition, the observed signal is assumed to be corrupted by an additive Gaussian white noise. Therefore, the measured discrete signal \mathbf{x} is written as:

$$\mathbf{x} = \mathbf{z} + \sigma \mathbf{w}, \quad (12)$$

where \mathbf{z} follows model (10), \mathbf{w} is a Gaussian white noise, whose variance is normalized to one. Thus, σ^2 denotes the variance of the additive noise $\sigma \mathbf{w}$.

B. Forecasting error

On the forecasting interval, we decompose the estimated signal $\tilde{\mathbf{x}}$ as follows:

$$\tilde{\mathbf{x}}[n] = \mathbf{z}[n] + \boldsymbol{\epsilon}[n], \quad (13)$$

where $\boldsymbol{\epsilon}$ is a the forecasting error. When $n \in I = \{0, \dots, N-1\}$, this error is only containing the measurement noise, that is $\boldsymbol{\epsilon}[n] = \sigma \mathbf{w}[n]$. Outside the interval I , the importance of the forecasting error $\boldsymbol{\epsilon}$ is also affected

by the loss of information resulting from the linearization of dynamical model we consider in (3). To evaluate the actual behavior of the forward forecasting error $\boldsymbol{\epsilon}[n]$ when $n \geq N$, we determine its two first moments.

- 1) The mean, which is also the estimation bias, is such that:

$$\begin{aligned} \boldsymbol{\mu}[n] &\triangleq \mathbb{E}\{\boldsymbol{\epsilon}[n]\} \\ &= \mathbb{E}\{\tilde{\mathbf{x}}[n]\} - \mathbf{z}[n]. \end{aligned}$$

Given the forecasting strategy, we have $\boldsymbol{\mu}[n] = 0$ when $n \in I$ and:

$$\boldsymbol{\mu}[n] = \mathbb{E}\{\boldsymbol{\alpha}^{(\ell)}\} \mathbf{z}_K + \sigma \mathbb{E}\{\boldsymbol{\alpha}^{(n-N+1)} \mathbf{w}_K\} - \mathbf{z}[n] \quad (14)$$

when $n \geq N$.

- 2) The covariance is given by:

$$\begin{aligned} \gamma[n, n'] &\triangleq \mathbb{E}\{(\boldsymbol{\epsilon}[n] - \boldsymbol{\mu}[n])(\boldsymbol{\epsilon}[n'] - \boldsymbol{\mu}[n'])\} \\ &= \mathbb{E}\{\tilde{\mathbf{x}}[n]\tilde{\mathbf{x}}[n']\} - \mathbf{z}[n]\mathbf{z}[n'] - \boldsymbol{\mu}[n]\mathbf{z}[n'] \\ &\quad - \boldsymbol{\mu}[n']\mathbf{z}[n] - \boldsymbol{\mu}[n]\boldsymbol{\mu}[n']. \end{aligned}$$

Thus by definition of the noise, we have $\gamma[n, n'] = \sigma^2 \delta_{n, n'}$ when $(n, n') \in I^2$. When $n \geq N$, let us denote $\ell = n - N + 1$. Then, we have two cases.

- (i) If $n' \in I$:

$$\begin{aligned} \gamma[n, n'] &= \sigma \mathbb{E}\{\mathbf{w}[n'] \boldsymbol{\alpha}^{(\ell)}\} \mathbf{z}_K + \sigma^2 \mathbb{E}\{\mathbf{w}[n'] \boldsymbol{\alpha}^{(\ell)} \mathbf{w}_K\} \\ &\quad - \mathbf{z}[n] \boldsymbol{\mu}[n'] - \boldsymbol{\mu}[n] \boldsymbol{\mu}[n']. \end{aligned} \quad (15)$$

- (ii) If $n' = N - 1 + \lambda \geq N$:

$$\begin{aligned} \gamma[n, n'] &= \mathbf{z}_K^T \mathbb{E}\{\boldsymbol{\alpha}^{(\ell)T} \boldsymbol{\alpha}^{(\lambda)}\} \mathbf{z}_K + \sigma \mathbb{E}\{\boldsymbol{\alpha}^{(\ell)} \mathbf{w}_K \boldsymbol{\alpha}^{(\lambda)}\} \mathbf{z}_K \\ &\quad + \sigma \mathbb{E}\{\boldsymbol{\alpha}^{(\lambda)} \mathbf{w}_K \boldsymbol{\alpha}^{(\ell)}\} \mathbf{z}_K + \sigma^2 \mathbb{E}\{\boldsymbol{\alpha}^{(\ell)} \mathbf{w}_K \boldsymbol{\alpha}^{(\lambda)} \mathbf{w}_K\} \\ &\quad - \mathbf{z}[n]\mathbf{z}[n'] - \mathbf{z}[n]\boldsymbol{\mu}[n'] - \mathbf{z}[n']\boldsymbol{\mu}[n] - \boldsymbol{\mu}[n]\boldsymbol{\mu}[n']. \end{aligned} \quad (16)$$

Besides, we recall that $\gamma[n, n'] = \gamma[n', n]$.

Expressions (14), (15), and (16) show that these quantities depend on the behavior of the forecasting random vector $\boldsymbol{\alpha}^{(\ell)}$. First, notice that the forecasting matrix $\tilde{\mathbf{A}}$ would ideally take the form:

$$\mathbf{A}_0 = \left(\frac{1}{K} \mathbf{Z}' \mathbf{Z}^T + \sigma^2 \mathbf{D}\right) \left(\frac{1}{K} \mathbf{Z} \mathbf{Z}^T + \sigma^2 \mathbf{I}\right)^{-1}, \quad (17)$$

with $\mathbf{Z} = (\mathbf{z}_0 \ \dots \ \mathbf{z}_{K-1})$ and $\mathbf{Z}' = (\mathbf{z}_1 \ \dots \ \mathbf{z}_K)$, where \mathbf{z}_k is the k -th sub-signal extracted from \mathbf{z} in the same way as \mathbf{x}_k is defined from \mathbf{x} in (2). Besides, $\mathbf{D} \in \mathbb{R}^{M \times M}$ is the Toeplitz matrix such that:

$$\mathbf{D}[m, m'] = \delta_{m+1, m'}.$$

Lemma 1 specify the asymptotic behavior of the forecasting vector $\boldsymbol{\alpha}^{(\ell)}$ when the dataset size K is great.

Lemma 1. Let \mathbf{x} be a random vector defined by (12). Let $\boldsymbol{\alpha}^{(\ell)}$ be the associated forecasting vector for the estimation of $\mathbf{x}[N-1+\ell]$, given by (6) and obtained from the least square

estimation (8). Let $\alpha_0^{(\ell)}$ be the last row of the ideal forecasting matrix \mathbf{A}_0^ℓ . Let $\mathbf{h}^{(\ell)}$ be the error vector given by:

$$\mathbf{h}^{(\ell)} = \alpha^{(\ell)} - \alpha_0^{(\ell)}.$$

Then, the random vector $\mathbf{h}^{(\ell)}$ converges in law to a zero-mean Gaussian random vector when $K \rightarrow \infty$, and we have:

$$\sqrt{K}\mathbf{h}^{(\ell)} \xrightarrow[K \rightarrow \infty]{\mathcal{D}} \mathcal{N}\left(\mathbf{0}, \mathbf{\Gamma}^{(\ell, \ell)}\right), \quad (18)$$

with $\mathbf{\Gamma}^{(\ell, \ell)} = \mathbf{F}^{(\ell)T} \mathbf{\Gamma}_0 \mathbf{F}^{(\ell)}$, where $\mathbf{\Gamma}_0 \in \mathbb{R}^{M(M+1) \times M(M+1)}$ is a covariance matrix and $\mathbf{F}^{(\ell)} \in \mathbb{R}^{M(M+1) \times M}$ is a Jacobian matrix. The expressions of these two matrices do not depend on K or σ .

Proof. See the Supplementary Material. The proof is based on the multivariate delta method (see paragraph 7.2 in [21]), which allows to asymptotically approximate a random vector normal as a Gaussian random vector. ■

Consequently, the covariance between $\sqrt{K}\mathbf{h}^{(\ell)}$ and $\sqrt{K}\mathbf{h}^{(\lambda)}$ remains bounded, i.e.:

$$K \mathbb{E} \left\{ \mathbf{h}^{(\ell)T} \mathbf{h}^{(\lambda)} \right\} \xrightarrow[K \rightarrow \infty]{} \mathbf{\Gamma}^{(\ell, \lambda)} = \mathbf{F}^{(\ell)T} \mathbf{\Gamma}_0 \mathbf{F}^{(\lambda)}.$$

Theorem 1. Let $\mathbf{x} \in \mathbb{R}^N$ be a discrete-time random signal following model (12). Let $\tilde{\mathbf{x}}$ denotes its forecasting, obtained using the extension Algorithm 1. Let $n \geq N$ be a sample index. Then, the first-order moment of the forecasting error $\epsilon[n]$ in (13) is approximated by:

$$\mu[n] \underset{K \rightarrow \infty}{\sim} o(\sigma^2) \quad (19)$$

Its second-order moment $\gamma[n, n']$ verify the following approximation equations:

(i) if $n' \in I = \{0, \dots, N-1\}$:

$$\gamma[n, n'] \underset{K \rightarrow \infty}{\sim} \sigma^2 \alpha_0^{(n-N-1)} [n' - (N-M)] \mathbb{1}_{(n' \geq N-M)} \quad (20)$$

(ii) if $n' \geq N$:

$$\gamma[n, n'] \underset{K \rightarrow \infty}{\sim} \frac{1}{K} \mathbf{z}_K^T \mathbf{\Gamma}^{(\ell, \lambda)} \mathbf{z}_K + \frac{\sigma^2}{K} \text{Tr} \left(\mathbf{\Gamma}^{(\ell, \lambda)} \right) + \sigma^2 \left\langle \alpha_0^{(\ell)}, \alpha_0^{(\lambda)} \right\rangle, \quad (21)$$

where $\ell = n - N + 1$ and $\lambda = n' - N + 1$.

Proof. See the Supplementary Material. The proof is mainly based on the results provided by Lemma 1, combined with the Isserlis' theorem [22], which provides a formula for the computation of higher-order moments of Gaussian random variables. ■

Ideally, the forecasting error would behave like the measurement noise $\sigma \mathbf{w}$, i.e. a zero-mean noise whose variance is of the order of σ^2 . Theorem 1 shows that the forecasting error is asymptotically unbiased. Concerning the covariance of the forecasting error, although equations (20) and (21) are not easily readable, one can evaluate the dependence of the variance in function of the tuning parameters, that are adjusted by the user. Let us focus on the forecasting error variance $\gamma[n, n]$ when

$n \geq N$. First, as expected, the variance increases linearly with the noise variance σ^2 . Second, it asymptotically depends linearly on the ratio $\frac{1}{K}$. This shows the need to use a sufficiently large dataset to obtain an accurate forecast. Third, the dependency on the sub-signals lengths M and the forecasting index $\ell = n - N + 1$ is hidden in the expression of the covariance matrix $\mathbf{\Gamma}^{(\ell, \ell)}$. We discuss this dependency in more detail in section IV-A1.

Remark 3 (AM-FM Model). One can extend the previous result to the case where the instantaneous frequencies and amplitudes of the components of the deterministic part of the observed signal are slowly varying. We therefore handle the AM-FM model which, in its continuous-time version, takes the following form:

$$z(t) = \sum_{j=1}^J a_j(t) \cos(2\pi\phi_j(t)), \quad (22)$$

where a_j and ϕ_j' are smooth function. These restrictions fixed on the variations of the instantaneous amplitudes and frequencies are specified by the so-called adaptive harmonic model (see [25] for example). In the case, the forecasting error is additionally sensitive to the speed of variation of the instantaneous amplitudes a_j and frequencies ϕ_j' .

C. Performance of the boundary effects reduction

Since it is beyond the scope of the present paper, we do not provide here a generic proof of the reduction of the boundary effects on any time-frequency representation. Let us focus instead on the particular case of synchrosqueezing transform. Since we analyze AM-FM signals, Theorem 1 ensures that the forecasting error ϵ defined in (13) is controlled and bounded in terms of mean and covariance. We can then rely on Theorem 3 in [23]. Indeed, this theorem states that when the additive noise remains small, the SST of the observed signal remains close to the ideal SST of an AM-FM signal, throughout the time-frequency plane. We refer the reader to [23] for a precise quantification of the error made in the time-frequency plane, which depends notably on the covariance of the additive noise and on the speed of variation of the amplitudes and instantaneous frequencies composing the signal. Therefore, in our case, this means that boundary effects are strongly reduced since instantaneous frequencies can now be approximately observed continuously up to the edges of the time-frequency plane.

The extension of this result to other time-frequency representations is not provided theoretically. In the following section IV, we verify experimentally that algorithm 2 is efficient for a large number of representations.

IV. NUMERICAL RESULTS

A. Evaluation the forecasting performance

In that section, we first evaluate the quality of the forecasting step and compare it to the theoretical results

provided by Theorem 1. The level of the forecasting error one depends on at least two parameters:

- The noise variance σ^2 .
- The size of the training dataset K .

In subsections IV-A1 and IV-A2, we study the influence of these parameters. A comparison with the theoretical results of section III is also available.

1) *Sum of sine waves*: We proved that the linear dynamic model is sufficient to catch the dynamical behavior of signals taking the form (10). In order to validate this theoretical result, we apply the forecasting Algorithm 1 to a large number of realizations of the random vector \mathbf{x} following the model (12), and such that the deterministic component \mathbf{z} takes the form:

$$\mathbf{z}[n] = \cos\left(2\pi p_1 \frac{n}{M}\right) + R \cos\left(2\pi p_2 \frac{n}{M}\right), \quad \forall n \in \{1, \dots, N\},$$

with $N = 10^4$, $M = 150$, $p_1 = 10$, $p_2 = 33$ and $R = 1.4$. Besides, the additive noise is chosen to be Gaussian: $\mathbf{w} \sim \mathcal{N}(\mathbf{0}, \mathbf{I})$.

a) *Influence of the noise variance σ^2* : Here, the size of the training dataset is set to $K = 450$. Then, the forecasting algorithm is run on 1000 realizations on the discrete signal \mathbf{x} for three different values of σ , logarithmically spaced from 10^{-3} to 10^{-1} . For each of these values, we determine the experimental bias $\mu_{xp}[N-1]$ and variance $\gamma_{xp}[N-1+\ell, N-1+\ell]$ in function of the forecasting sample index ℓ (going from 1 to $L = 100$).

The experimental results show that the bias is neither depending on the noise variance σ^2 nor the forecasting length ℓ . Indeed, independently of σ , we always have $\mu_{xp}[N-1+\ell] \in [-0.03\sigma, 0.03\sigma]$, which is negligible with respect to the magnitude of \mathbf{z} . This result confirms the theoretical result (19).

On Fig. 2, we display the experimental variance $\gamma_{xp}[N-1+\ell, N-1+\ell]$ for each value of σ (+ markers). The associated theoretical asymptotic forecasting variance (21) is also displayed in solid line. As expected, this result highlights the fact that the forecasting variance increases linearly with respect to σ^2 . More surprisingly, this result shows that the forecasting variance slightly decreases with ℓ , what is counterintuitive. It should be noted that, contrary to what expression (21) suggests, smaller values of σ do not cause a decrease of the experimental variance, but an increase. This comes from the fact that when σ is small, the matrix $\mathbf{X}\mathbf{X}^T$ becomes ill-conditioned. The calculation of the forecasting matrix $\tilde{\mathbf{A}}$ in (8) is then strongly disturbed.

b) *Influence of the training dataset size K* : Here, the noise variance σ is set to $\sigma = 10^{-2}$. Then, the forecasting algorithm is run on 3000 realizations on the discrete signal \mathbf{x} for three different values of K , logarithmically spaced from 4.5×10^2 to 2×10^3 . For each of these values, we determine the experimental bias $\mu_{xp}[N-1+\ell]$ and variance $\gamma_{xp}[N-1+\ell, N-1+\ell]$ in function of the forecasting sample index ℓ (going from 1 to 500).

As in the previous study, the experimental bias vanishes when K increases, what confirms the approxima-

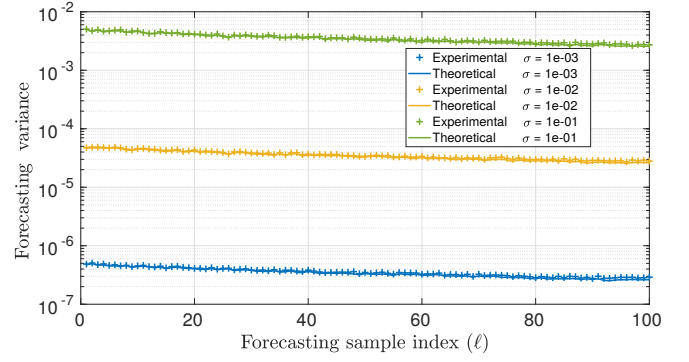


Figure 2. Evolution of the experimental and theoretical forecasting variance in function of the forecasting sample index for different values of σ .

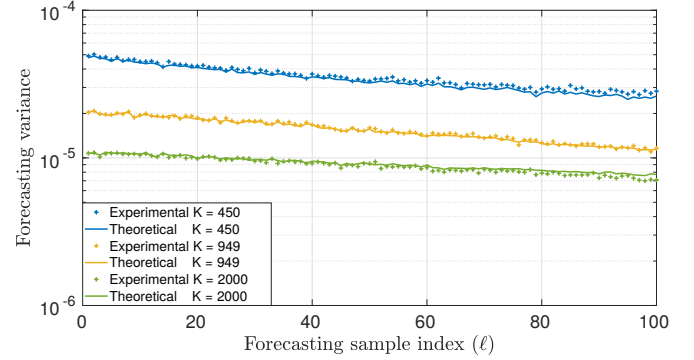


Figure 3. Evolution of the experimental and theoretical forecasting variance in function of the forecasting sample index for different values of K .

tion result (19). Besides, the experimental variance is displayed on Fig. 3 (+ markers), and compared with the associated theoretical variance (21). Each color corresponds to these experimental results obtained for a given value of K . This result validates the asymptotic behavior provided by (21), and we can show that, as soon as K is sufficiently high, the product $K\gamma[\ell, \ell]$ is approximately independent of K .

c) *Summary*: Both previous experimental results combined with the theoretical asymptotic equation (21) allow us to describe the influence of the noise variance and the size of the training dataset on the variance of the forecasting noise, which is empirically summarized as follows:

$$\gamma[N-1+\ell, N-1+\ell] \underset{K \rightarrow \infty}{\approx} \frac{\sigma^2}{K} g[\ell]. \quad (23)$$

where g is a bounded positive function. The empirical result is coherent with the theoretical result provided by Theorem 1.

This study neglects the analysis of the influence of the parameter M , whose influence on the value of the experimental variance is numerically not significant as long as $M \ll 2K$. The choice of this parameter is especially crucial when the deterministic component of the signal is no longer stationary. The adaptive harmonic model, discussed below, is an example.

2) *Adaptive harmonic model*: We now consider a signal whose instantaneous frequencies and amplitudes of its components vary over time. The deterministic component \mathbf{z} of the random vector \mathbf{x} (constructed following the model (12)) takes the following form, for all $n \in \{1, \dots, N\}$:

$$\mathbf{x}[n] = \cos(2\pi\phi_1[n]) + R[n] \cos(2\pi\phi_2[n]) ,$$

where the instantaneous amplitude R is given by:

$$R[n] = 1.4 + 0.2 \cos\left(4\pi \frac{n}{N}\right) ,$$

and the instantaneous phases are such that:

$$\begin{aligned} \phi_1[n] &= \frac{p_1}{M} \left(n + \frac{0.01}{2\pi} \cos\left(2\pi \frac{n}{N}\right) \right) \\ \phi_2[n] &= p_2 \frac{n}{M} + \frac{20}{2Nf_s} n^2 \end{aligned}$$

Besides, the additive noise is chosen to be Gaussian: $\mathbf{w} \sim \mathcal{N}(\mathbf{0}, \mathbf{I})$. Numerically, we take: $N = 10^4$, $M = 750$, $p_1 = 10$, $p_2 = 23$.

To highlight the fact that the linear dynamical model is sufficient to catch most of the dynamical behavior of signals following the AHM, we compare the performance of the Algorithm 2 with reference forecasting algorithm that could be used for extending such signals. These methods are:

- The *Extended Dynamic Mode Decomposition (EDMD)* has been developed by Williams *et al.* [16]. The proposed algorithm is a way to obtain an approximation of the so-called Koopman operator of the observed system, which theoretically allows to catch dynamic of nonlinear systems [24].
- The *Gaussian Process Regression (GPR)* [17] is a method relying on a probabilistic dynamical model. That one is based on the Gaussian process structure, and therefore offer more flexibility in the type of dynamic that could be modeled than the linear model (3).
- The *Trigonometric, Box-Cox transformation, ARMA errors, Trend and Seasonal components (TBATS)* method [19] is based on a classical decomposition of times series into a trend, a seasonal and an ARMA components, with a specific dynamic for the seasonal component. This model demands the estimation of numerous parameters and, by implication, may be slow.

To quantify the global quality (i.e. not depending on ℓ) of the forecasting approaches, we evaluate the Experimental Mean Square Error $\text{MSE}_{\text{xp}}(\tilde{\mathbf{x}})$ of the forward forecast extended signals, namely:

$$\begin{aligned} \text{MSE}_{\text{xp}}(\tilde{\mathbf{x}}) &= \frac{1}{L} \|\tilde{\mathbf{x}} - \mathbf{x}^{\text{ext}}\|^2 \\ &= \frac{1}{L} \sum_{\ell=1}^L \mu_{\text{xp}}[N-1+\ell]^2 + \gamma_{\text{xp}}[N-1+\ell, N-1+\ell]. \end{aligned} \quad (24)$$

where \mathbf{x}^{ext} is the ground-truth extended signal, that is: $\mathbf{x}^{\text{ext}} = (\mathbf{x}[-L] \ \dots \ \mathbf{x}[N-1+L])$. Then, as long as the

Table I
AHM SIGNAL. PERFORMANCE OF THE EXTENSION METHODS.

Algorithm	MSE		Computing time (sec.)
	Mean	Standard deviation	
SigExt	1.433×10^{-3}	4.361×10^{-4}	0.15
EDMD	3.076×10^{-2}	8.095×10^{-2}	2.53
GPR	1.436×10^{-3}	4.346×10^{-4}	146.33
TBATS	1.732×10^{-3}	4.924×10^{-4}	1837.12

bias $\mu[N-1+\ell]$ and the variance $\gamma[N-1+\ell, N-1+\ell]$ of the forecasting estimator remain small for all ℓ , the MSE takes small values either. Corresponding results are given in Table I. They show that the naive extension we propose gives satisfying results, even though the other methods, more sophisticated, give MSE values that are somewhat smaller. Nevertheless, a major limit of those methods is the computing time they require, which prevent them from being used to exploit real-time data. Thus, SigExt is the extension method that optimize the trade-off between the forecasting quality and the computing time. That is why, it is implemented in our algorithm for the reduction of boundary effects.

B. Evaluation of the quality of the boundary effects reduction

1) *Metrics*: The quality of the boundary effects reduction must be evaluated directly on the time-frequency representation. To that aim, we compare the obtained representation to the optimal representation $\mathcal{F}_N^{\text{opt}}(\mathbf{x})$. The optimal representation is defined as the restriction of the representation of the ground-truth extended signal \mathbf{x}^{ext} . Therefore, we have:

$$\mathcal{F}_N^{\text{opt}}(\mathbf{x}) = \mathcal{R}(\mathcal{F}_{N+2L}(\mathbf{x}^{\text{ext}})) .$$

In the aim of comparing the different techniques, we use a criterion, proposed in [25], that quantify the distance between a given time-frequency representation and the optimal one. It is built in analogy with the optimal transport distance, which enables quantifying the distance between two probability density functions. Let us generically denote a time frequency representation \mathcal{Q} . Then, for t fixed, we consider the following pseudo-probability density function:

$$p_{\mathcal{Q}}^t(\xi) = \frac{|\mathcal{Q}(\xi, t)|^2}{\int_{\mathbb{R}} |\mathcal{Q}(\nu, t)|^2 d\nu} . \quad (25)$$

Then, at each instant t , we can then determine the optimal transport distance d_t between the two pseudo densities. It is given by the L^1 norm of the difference between the associated distribution functions. In other words, we have:

$$d_t(\mathcal{Q}, \mathcal{F}_0) = \int_{\mathbb{R}} |\tilde{P}_{\mathcal{Q}}^t(\xi) - P_{\mathcal{F}_0}^t(\xi)| d\xi ,$$

where $P_{\mathcal{Q}}^t(\xi) = \int_{-\infty}^{\xi} p_{\mathcal{Q}}^t(\nu) d\nu$ and $\tilde{P}_{\mathcal{F}_0}^t(\xi) = \int_{-\infty}^{\xi} \tilde{p}_{\mathcal{F}_0}^t(\nu) d\nu$. Finally, the distance between the two

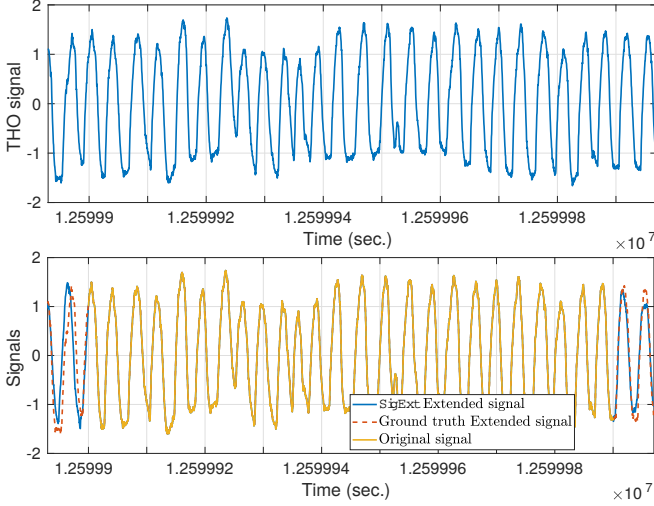


Figure 4. Zoom on the respiratory signal. Top: original measured signal. Extended signal obtained by SigExt forecasting superimposed with the ground truth signal.

time-frequency representations is obtained by averaging all the optimal transport distances with respect to time:

$$D(\mathcal{Q}, \mathcal{F}_0) = \frac{1}{|I|} \int_I d_t(\mathcal{Q}, \mathcal{F}_0) dt. \quad (26)$$

The *Optimal Transport Distance* (OTD) quantifies the proximity between the estimated and actual instantaneous frequencies while favouring the sparsity of the estimated time-frequency representation.

Let us evaluate the quality of the boundary effects reduction on biomedical signals.

2) *Respiratory signal*: We first consider a 50 minutes-long respiratory signal. This signal is sampled at $f_s = 100$ Hz. A zoom on a small portion of the signal is displayed in Fig. 4.

From that large signal, we build a dataset of 48 non-overlapping signals of 60 seconds, i.e. $N = 6000$. On each of these pieces of signal, we implement the forecasting method introduced in section IV-A2, including the SigExt method detailed in Algorithm 1. However, the TBATS extension method is not implemented here because of its excessive computing time. The extensions of 7 seconds-long on each boundary, corresponding to $L = 700$. Thus, in order to catch slowly varying dynamical behaviors, the size of the training signal M is chosen so that $M = \lfloor 1.5L \rfloor$. As a result of section IV-A1, we take: $K = \lfloor 2.5M \rfloor$. The average and the median of the MSE (24) with respect to the simulations are given in Table II. The averaged MSE of SigExt method is overwhelmingly higher than the averaged MSE of the other methods. This result is caused by the presence of outliers in some extensions by SigExt. Indeed, the value median of the MSE is of the same order than those of the other methods. These outliers are probably due to the presence of pulse in the respiratory signal. That ones make the AM-FM model temporarily irrelevant, and break the validity of the linear dynamical model (3)

Table II
RESPIRATORY SIGNAL. MSE OF THE RESPIRATORY SIGNAL EXTENSIONS.

Algorithm	MSE	
	Mean	Median
SigExt	1.704×10^1	7.346×10^{-1}
EDMD	2.172×10^{-2}	7.349×10^{-1}
GPR	4.476×10^{-2}	1.998×10^{-2}

Table III
RESPIRATORY SIGNAL. AVERAGED OTD OF THE BOUNDARY EFFECTS REDUCTION METHODS ON DIVERSE REPRESENTATIONS.

Extension method	Time-Frequency Representation			
	STFT	SST	RS	ConceFT
Without extension	2.16×10^{-2}	5.26×10^{-3}	3.07×10^{-2}	1.41×10^{-2}
SigExt	1.72×10^{-2}	4.00×10^{-3}	2.43×10^{-2}	1.12×10^{-2}
EDMD	1.75×10^{-2}	4.23×10^{-3}	2.45×10^{-2}	1.14×10^{-2}
GPR	1.84×10^{-2}	4.10×10^{-3}	2.48×10^{-2}	1.10×10^{-2}

used to extend the signal. That is why SigExt is less robust to the vanishing of oscillations that the GPR or EDMD extensions.

Then, we apply the boundary effects reduction method BoundEffRed (Algorithm 2) on these extensions for diverse time-frequency representations: STFT, SST, RS, as well as ConceFT, an SST-based representation introduced in [25]. In Table III, the results are compared in terms of OTD. They are also compared with the strategy consisting in a zero-padding extension of the signal. Even though the performance of the forecasting Algorithm 1 is somehow moderate, the boundary effects can be reduced dramatically on the time-frequency representations. Notice that the extension length L has been set accordingly to the window length used by the time-frequency analysis tool. For instance, here the window length we use to evaluate the STFT is of 1500 samples. To prevent the STFT from being sensitive to the boundary effects, we set $L = 750$. In this way, when evaluating the spectral content of the signal near its boundaries, the analysis is not limited by a lack of information all along the window support. From now on, all results are given for L at equal to the half of the width of the window used in the time-frequency transform.

3) *Photoplethysmogram*: We perform a study similar to the previous one on a 640 second-long photoplethysmogram (PPG) signal, sampled at $f_s = 125$ Hz. A 32 second-long piece of this signal is displayed on the top of Fig. 5. The estimated 2-second extension obtained by SigExt on both boundary of this signal is superimposed to the ground-truth signal in the bottom of Fig. 5.

We divide the signal into 32-second long pieces, and apply Algorithm 2 on each piece. We provide in Table IV the OTD to the optimal time-frequency representation averaged over the signals. For all the considered time-frequency representations, the results clearly shows that our algorithm reduce the influence of the boundary effects. This highlights the ability of our approach to limit

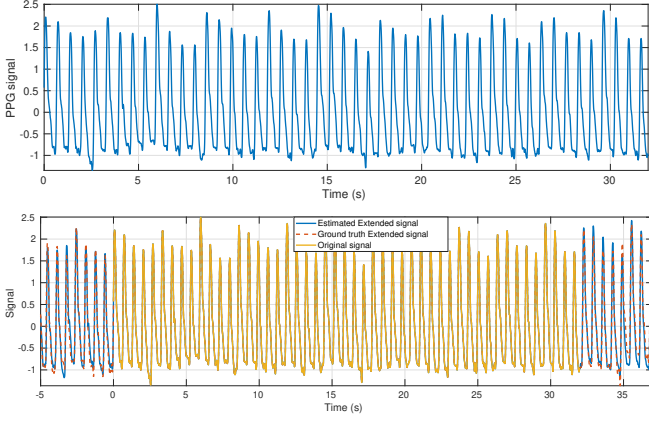


Figure 5. PPG signal. Top: original measured signal. Extended signal obtained by forecasting superimposed with the ground truth signal.

Table IV
PPG SIGNAL. AVERAGED OTD OF THE BOUNDARY EFFECTS
REDUCTION METHODS ON DIVERSE REPRESENTATIONS.

Extension method	Time-Frequency Representation		
	STFT	SST	RS
Without extension	2.52×10^{-2}	9.41×10^{-2}	1.03×10^{-1}
SigExt	1.22×10^{-3}	7.31×10^{-2}	1.11×10^{-1}
EDMD	9.83×10^{-4}	5.59×10^{-2}	9.80×10^{-2}
GPR	1.14×10^{-3}	7.02×10^{-2}	1.07×10^{-1}

the distortion due the boundary effects and provide a more accurate representations. Even though the SIGEXT extension yields time-frequency representations slightly more sensitive to boundary effects that the extensions given by EDMD or GPR, it is the only technique that allows a real-time implementation.

On Fig. 6, we display the SST resulting from the BoundEffRed strategy, applied to the same portion of PPG than what is used to display Fig. 5. We clearly observe an improvement of the quality of the SST near boundaries. Indeed, the blurring visible when zooming on the right boundary of the SST has almost vanished (see bottom of Fig. 6). The real-time tracking of the instantaneous frequencies contained in the measured signal is therefore largely facilitated.

To evaluate the influence of the noise level on the performance of BoundEffRed, we artificially add a Gaussian noise to the measured PPG signal, whose variance is denoted σ_{add}^2 . It is thus an additional noise to the measurement noise actually contained in the signal. Fig. 7 shows the averaged OTD of BoundEffRed for different values of σ_{add}^2 . At first glance, we notice that STFT is slightly more sensitive to noise than SST or RS. On one hand, the robustness to noise of the SST and the RS is the direct consequence of the approximation result of [25], discussed in section III-C. On the other hand, the sensitivity to noise of the STFT may be interpreted as the inability to forecast the values of the time-frequency coefficients where only noise is active, while sharp time-frequency representations, such as SST or RS, ideally vanish at these points.

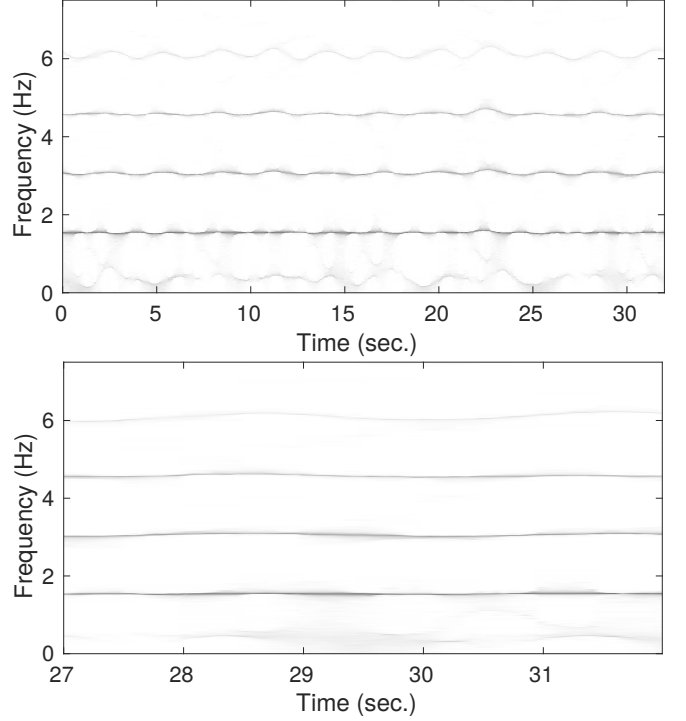


Figure 6. Result of BoundEffRed on the synchrosqueezing transform of a PPG (top) with a zoom on its right boundary (bottom).

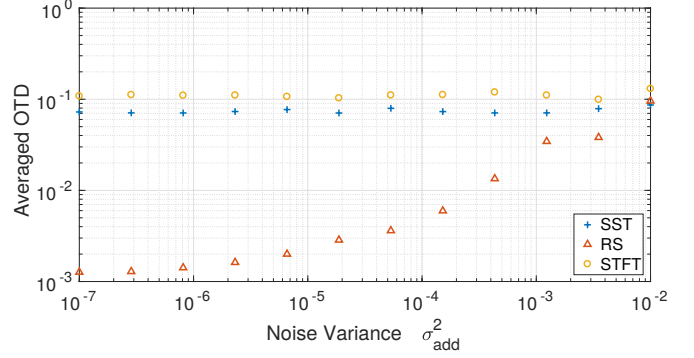


Figure 7. PPG signal. Averaged OTD of BoundEffRed in function of the noise variance.

V. CONCLUSION

In this paper, we propose an algorithm, named BoundEffRed, for the boundary effects reduction on time-frequency representations. This method is based on an extension of the signal obtained by forecasting. We have shown theoretically that the chosen dynamic model is sufficient for the extension of signals formed by a sum of sine waves whose instantaneous frequencies and amplitudes vary slowly. Moreover, the numerical results show that this strategy allows us to switch to a real-time implementation of BoundEffRed is possible, due to the low computation time, unlike other pre-existing forecasting methods. The numerical results also confirmed the robustness to noise of BoundEffRed, as well as its ability to be applied to many time-frequency representations. The MATLAB code and datasets used to produce the

numerical results of this paper are available online at the following address:

<https://github.com/AdMeynard/BoundaryEffectsReduction>

Other numerical examples are also included, such as the application of BoundEffRed to other types of biomedical signals such as ECGs.

Various improvements can be considered to make the algorithm more robust to certain situations. In particular, we have noticed that when the observed signal does not oscillate, the forecasting is no longer relevant, and outlier time-frequency representations are obtained. A preliminary step should then be added to the algorithm to select the portions of the signal that exhibit oscillations, in order to reject the portions for which accurate time-frequency analysis is practically useless. A more fundamental improvement would be to perform the prediction step directly in the time-frequency plane, with the aim of specifically predicting the evolution of each instantaneous frequency. This would lead to seeing a time-frequency representation as a set of interdependent time series (corresponding to each frequency band).

REFERENCES

- [1] D. Stowell, *Computational Analysis of Sound Scenes and Events*. Springer, 2018, ch. Computational Bioacoustic Scene Analysis, pp. 303–333.
- [2] M. Müller, D. P. W. Ellis, A. Klapuri, and G. Richard, “Signal processing for music analysis,” *IEEE Journal of Selected Topics in Signal Processing*, vol. 5, no. 6, pp. 1088–1110, 2011.
- [3] Z. Peng, F. Chu, and Y. He, “Vibration signal analysis and feature extraction based on reassigned wavelet scalogram,” *Journal of Sound and Vibration*, vol. 253, no. 5, pp. 1087 – 1100, 2002. [Online]. Available: <http://www.sciencedirect.com/science/article/pii/S0022460X01940854>
- [4] M. Akay, *Detection and Estimation Methods for Biomedical Signals*, 1st ed. USA: Academic Press, Inc., 1996.
- [5] P. Stoica and R. Moses, *Spectral analysis of signals*. Upper Saddle River, N.J.: Pearson/Prentice Hall, 2005.
- [6] G. Matz, F. Hlawatsch, and W. Kozek, “Generalized evolutionary spectral analysis and the Weyl spectrum of nonstationary random processes,” *IEEE Transactions on Signal Processing*, vol. 45, no. 6, pp. 1520–1534, Jun. 1997.
- [7] K. Gröchenig, *Foundations of time-frequency analysis*, ser. Applied and Numerical Harmonic Analysis. Boston, MA: Birkhäuser Inc., 2001.
- [8] S. Mallat, *A Wavelet Tour of Signal Processing (Second Edition)*. San Diego: Academic Press, 1999.
- [9] F. Auger, P. Flandrin, Y.-T. Lin, S. McLaughlin, S. Meignen, T. Oberlin, and H.-T. Wu, “Time-frequency reassignment and synchrosqueezing: An overview,” *IEEE Signal Processing Magazine*, vol. 30, no. 6, pp. 32–41, 2013.
- [10] N. Delprat, B. Escudié, P. Guillemain, R. Kronland-Martinet, P. Tchamitchian, and B. Torrèsani, “Asymptotic wavelet and Gabor analysis: extraction of instantaneous frequencies,” *IEEE Transactions on Information Theory*, vol. 38, no. 2, pp. 644–664, Mar. 1992.
- [11] C. K. Chui and E. Quak, *Numerical Methods in Approximation Theory*, ser. ISNM 105: International Series of Numerical Mathematics. Basel: Birkhäuser, 1992, vol. 9, ch. Wavelets on a Bounded Interval, pp. 53–75.
- [12] U. Depczynski, K. Jetter, K. Molt, and A. Niemöller, “The fast wavelet transform on compact intervals as a tool in chemometrics: II. Boundary effects, denoising and compression,” *Chemometrics and Intelligent Laboratory Systems*, vol. 49, no. 2, pp. 151 – 161, 1999. [Online]. Available: <http://www.sciencedirect.com/science/article/pii/S0169743999000374>
- [13] I. Kharitonenko, X. Zhang, and S. Twelves, “A wavelet transform with point-symmetric extension at tile boundaries,” *IEEE Transactions on Image Processing*, vol. 11, no. 12, pp. 1357–1364, 2002.
- [14] L. Chen, T. Q. Nguyen, and K.-P. Chan, “Symmetric extension methods for m-channel linear-phase perfect-reconstruction filter banks,” *IEEE Transactions on Signal Processing*, vol. 43, no. 11, pp. 2505–2511, 1995.
- [15] J. R. Williams and K. Amaratunga, “A discrete wavelet transform without edge effects using wavelet extrapolation,” *The Journal of Fourier Analysis and Applications*, vol. 3, pp. 435–449, 1997.
- [16] M. O. Williams, I. G. Kevrekidis, and C. W. Rowley, “A Data-Driven Approximation of the Koopman Operator: Extending Dynamic Mode Decomposition,” *Journal of Nonlinear Science*, vol. 25, pp. 1307–1346, 2015.
- [17] C. E. Rasmussen and C. K. I. Williams, *Gaussian Processes for Machine Learning*, ser. Adaptive Computation and Machine Learning series. The MIT Press, 2006.
- [18] S. Roberts, M. Osborne, M. Ebden, S. Reece, N. Gibson, and S. Aigrain, “Gaussian processes for time-series modelling,” *Philosophical Transactions of the Royal Society A: Mathematical, Physical and Engineering Sciences*, vol. 371, no. 1984, p. 20110550, 2013. [Online]. Available: <https://royalsocietypublishing.org/doi/abs/10.1098/rsta.2011.0550>
- [19] A. M. D. Livera, R. J. Hyndman, and R. D. Snyder, “Forecasting time series with complex seasonal patterns using exponential smoothing,” *Journal of the American Statistical Association*, vol. 106, no. 496, pp. 1513–1527, 2011. [Online]. Available: <https://doi.org/10.1198/jasa.2011.tm09771>
- [20] P. J. Schmid, “Dynamic mode decomposition of numerical and experimental data,” *Journal of Fluid Mechanics*, vol. 656, pp. 5–28, 2010.
- [21] J. Alho and B. Spencer, *Statistical Demography and Forecasting*, ser. Springer Series in Statistics. Springer-Verlag New York, 2005.
- [22] L. Isserlis, “On a formula for the product-moment coefficient of any order of a normal frequency distribution in any number of variables,” *Biometrika*, vol. 12, no. 1-2, pp. 134–139, 11 1918. [Online]. Available: <https://doi.org/10.1093/biomet/12.1-2.134>
- [23] Y.-C. Chen, M.-Y. Cheng, and H.-T. Wu, “Non-parametric and adaptive modelling of dynamic periodicity and trend with heteroscedastic and dependent errors,” *Journal of the Royal Statistical Society Series B*, vol. 76, no. 3, pp. 651–682, June 2014. [Online]. Available: <https://ideas.repec.org/a/bla/jorssb/v76y2014i3p651-682.html>
- [24] M. Korda and I. Mezić, “Linear predictors for nonlinear dynamical systems: Koopman operator meets model predictive control,” *Automatica*, vol. 93, pp. 149 – 160, 2018. [Online]. Available: <http://www.sciencedirect.com/science/article/pii/S000510981830133X>
- [25] I. Daubechies, Y. G. Wang, and H.-T. Wu, “ConceFT: concentration of frequency and time via a multitapered synchrosqueezed transform,” *Philosophical Transactions of the Royal Society A: Mathematical, Physical and Engineering Sciences*, vol. 374, no. 2065, p. 20150193, 2016. [Online]. Available: <https://royalsocietypublishing.org/doi/abs/10.1098/rsta.2015.0193>